



Multiscale Modeling of Armor Ceramics: Focus on AlON

**by G. A. Gazonas, J. W. McCauley, I. G. Batyrev, D. Casem, J. D. Clayton,
D. P. Dandekar, R. Kraft, B. M. Love, B. M. Rice, B. E. Schuster,
and N. S. Weingarten**

ARL-RP-337

September 2011

A reprint from Proceedings of the 27th Army Science Conference, Orlando, FL, 29 November 2010.

NOTICES

Disclaimers

The findings in this report are not to be construed as an official Department of the Army position unless so designated by other authorized documents.

Citation of manufacturer's or trade names does not constitute an official endorsement or approval of the use thereof.

Destroy this report when it is no longer needed. Do not return it to the originator.

Army Research Laboratory

Aberdeen Proving Ground, MD 21005-5069

ARL-RP-337**September 2011**

Multiscale Modeling of Armor Ceramics: Focus on AlON

**G. A. Gazonas, J. W. McCauley, I. G. Batyrev, D. Casem, J. D. Clayton,
D. P. Dandekar, R. Kraft, B. M. Love, B. M. Rice, B. E. Schuster,
and N. S. Weingarten
Weapons and Materials Research Directorate, ARL**

A reprint from Proceedings of the 27th Army Science Conference, Orlando, FL, 29 November 2010.

REPORT DOCUMENTATION PAGE				Form Approved OMB No. 0704-0188	
Public reporting burden for this collection of information is estimated to average 1 hour per response, including the time for reviewing instructions, searching existing data sources, gathering and maintaining the data needed, and completing and reviewing the collection information. Send comments regarding this burden estimate or any other aspect of this collection of information, including suggestions for reducing the burden, to Department of Defense, Washington Headquarters Services, Directorate for Information Operations and Reports (0704-0188), 1215 Jefferson Davis Highway, Suite 1204, Arlington, VA 22202-4302. Respondents should be aware that notwithstanding any other provision of law, no person shall be subject to any penalty for failing to comply with a collection of information if it does not display a currently valid OMB control number. PLEASE DO NOT RETURN YOUR FORM TO THE ABOVE ADDRESS.					
1. REPORT DATE (DD-MM-YYYY) September 2011		2. REPORT TYPE Reprint		3. DATES COVERED (From - To) January 2009–October 2010	
4. TITLE AND SUBTITLE Multiscale Modeling of Armor Ceramics: Focus on AION				5a. CONTRACT NUMBER	
				5b. GRANT NUMBER	
				5c. PROGRAM ELEMENT NUMBER	
6. AUTHOR(S) G. A. Gazonas, J. W. McCauley, I. G. Batyrev, D. Casem, J. D. Clayton, D. P. Dandekar, R. Kraft, B. M. Love, B. M. Rice, B. E. Schuster, and N. S. Weingarten				5d. PROJECT NUMBER AH42	
				5e. TASK NUMBER	
				5f. WORK UNIT NUMBER	
7. PERFORMING ORGANIZATION NAME(S) AND ADDRESS(ES) U.S. Army Research Laboratory ATTN: RDRL-WMM-D Aberdeen Proving Ground, MD 21005-5069				8. PERFORMING ORGANIZATION REPORT NUMBER ARL-RP-337	
9. SPONSORING/MONITORING AGENCY NAME(S) AND ADDRESS(ES)				10. SPONSOR/MONITOR'S ACRONYM(S)	
				11. SPONSOR/MONITOR'S REPORT NUMBER(S)	
12. DISTRIBUTION/AVAILABILITY STATEMENT Approved for public release; distribution is unlimited.					
13. SUPPLEMENTARY NOTES A reprint from <i>Proceedings of the 27th Army Science Conference</i> , Orlando, FL, 29 November–2 December 2010.					
14. ABSTRACT The computational modeling linkage from the atomistic to the continuum scales of homogeneous and discrete deformation mechanisms (twinning, cleavage, micro-cracking, stacking faults, et cetera), nano- and microstructure and defects, to dynamic failure processes in brittle materials should provide pathways to designing improved mechanical performance through controlled processing. This report will review results from an internal multiscale computational program in first-principles design of armor ceramics, with a focus on an optically transparent armor ceramic, polycrystalline (~200 µm grain size) aluminum oxynitride (AION) spinel, that uses a multiscale modeling approach, and will overview the special computational challenges that are required for linking the vast spatiotemporal scales from the quantum to the continuum. The GRAND CHALLENGE is to be able to design materials atom by atom and to predict performance.					
15. SUBJECT TERMS brittle failure, AION, hierarchical, concurrent, verification and validation					
16. SECURITY CLASSIFICATION OF:			17. LIMITATION OF ABSTRACT UU	18. NUMBER OF PAGES 16	19a. NAME OF RESPONSIBLE PERSON George Gazonas
a. REPORT Unclassified	b. ABSTRACT Unclassified	c. THIS PAGE Unclassified			19b. TELEPHONE NUMBER (Include area code) 410-306-0863

MULTISCALE MODELING OF ARMOR CERAMICS: FOCUS ON AION

G. A. Gazonas*, J. W. McCauley, I. G. Batyrev, D. Casem, J. D. Clayton,
D. P. Dandekar, R. Kraft, B. M. Love, B. M. Rice, B. E. Schuster, N. S. Weingarten

U.S. Army Research Laboratory
Weapons and Materials Research Directorate
Aberdeen Proving Ground, Maryland 21005-5066

ABSTRACT

The computational modeling linkage from the atomistic to the continuum scales of homogeneous and discrete deformation mechanisms (twinning, cleavage, micro-cracking, stacking faults, et cetera), nano- and microstructure and defects, to dynamic failure processes in brittle materials should provide pathways to designing improved mechanical performance through controlled processing. This paper will review results from an internal multiscale computational program in first-principles design of armor ceramics, with a focus on an optically transparent armor ceramic, polycrystalline ($\sim 200 \mu\text{m}$ grain size) aluminum oxynitride (AION) spinel, that uses a multiscale modeling approach, and will overview the special computational challenges that are required for linking the vast spatiotemporal scales from the quantum to the continuum. The GRAND CHALLENGE is to be able to design materials atom by atom and to predict performance.

1. INTRODUCTION

The computational bridge between the atomistic and continuum length scales is addressed in a hierarchical fashion (Fig. 1) through development of: 1) a first principles unit cell model to predict the anisotropic elastic properties of AION, 2) a classical molecular dynamics model through periodic replication of the unit cell model for the study of single crystal slip and twinning dynamics, 3) a single crystal anisotropic plasticity model to account for the kinematics of crystal slip and twinning mechanisms in AION, 4) a mesoscopic polycrystalline computational finite element model that incorporates single crystal deformation kinematics, and explicitly includes microcracks that are represented on the grain boundaries using cohesive interface laws that allow investigation of crack nucleation, growth, and coalescence, and 5) a continuum computational finite element model with the particular challenge of development of algorithms for transitioning microcrack coalescence behavior at the mesoscale to the continuum.

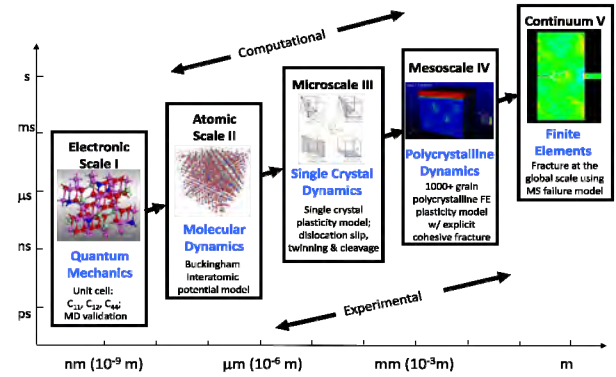


Fig. 1. A multiscale constitutive and failure model for AION that illustrates the spatiotemporal dependence of the scales.

Critical in the development of the hierarchical multiscale model outlined above is the experimental validation of the individual scales. Quantum and molecular dynamics predictions of the three independent anisotropic elastic constants of AION, C_{11} , C_{12} , C_{44} , should be consistent with each other, and with experimentally determined values on few tens of micron size oriented single crystals of AION, using for example, Brillouin spectroscopy or focused-ion-beam (FIB)/SEM compression and tension tests. The chief challenge for modeling brittle armor materials is to correctly account for the growth kinetics of microcracks, inelastic deformation mechanisms, and the influence of defects in a multiscale computational environment. The propagation of microcracks at smaller scales will be "coarse-grained," to higher scales where global fracture failure and fragmentation is observed. Such coarse graining algorithms can be validated through continuum-scale experiments that measure dynamic crack propagation speeds, mixed-mode failure, and crack bifurcation phenomena using the in-house coherent gradient sensing (CGS) and/or high speed imaging techniques. The development of consistent coarse-graining algorithms for fracture and other localization phenomena, which are associated with failure and loss of material stability, is a relatively unexplored but critical aspect of this research.

2. EXPERIMENTAL OBSERVATIONS

2.1 Dynamic Fracture and Inelastic Deformation

The complex fracture patterns that are observed in polycrystalline AlON from an Edge-on-Impact (EOI) by a spherical steel impactor travelling at ~ 430 m/s reveal the multiscale nature of fracture in AlON (Fig. 2).

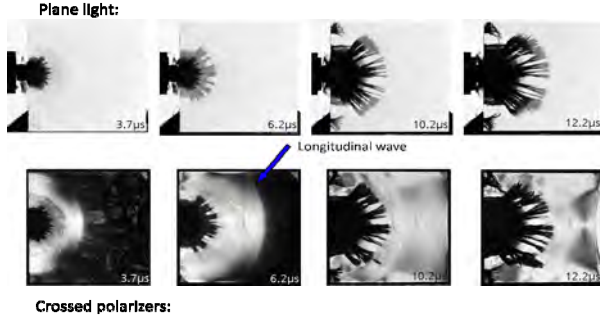


Fig. 2. Shadowgraphs corresponding to photographs at various times after impact from a spherical projectile (Strassburger et al., 2006).

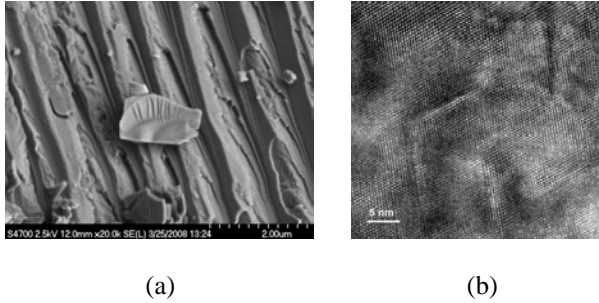


Fig. 3. a) SEM of microcleavage fracture from an EOI test, b) HRTEM showing a high density of dissociated $\langle 110 \rangle$ dislocations along $\{111\}$ planes have been identified.

A scanning electron micrograph (SEM) image of fracture surfaces of post mortem samples of AlON from an EOI experiment (Fig. 3(a)) illustrate the complex nano- and micro-cleavage patterns from these dynamic tests. Chen and McCauley are also carrying out systematic indentation studies on single crystal AlON grains to determine the deformation mechanisms in an intrinsically confined test. A high resolution transmission electron microscopy (HRTEM) image of a cross section through an AlON indentation is illustrated in Fig. 3(b).

In addition to dynamic compressive strength measurements carried out in a Kolsky bar arrangement, impact transitional velocity measurements are also being determined. Fig. 4 shows a flash X-ray radiograph of

AlON being penetrated during this test. The transitional velocity was measured as 1207 m/s. Of course, a major challenge is to predict these experimental observations using the multiscale modeling and simulation approach.

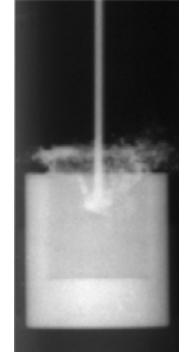


Fig. 4. X-ray radiograph of penetration into AlON above transitional velocity (Lundberg and Andersson, 2010).

2.2 FIB/SEM Experiments

We have developed a custom test apparatus for in-situ scanning electron microscope (SEM) mechanical testing. Our system utilizes a 5-axis piezoelectric positioning system that enables precise placement and alignment of the micro-specimens, either within the tensile grip or near the compression platen. Loads are applied using a high-resolution linear actuator with a reported resolution of ~ 1 nm and measured with a strain gage based S-beam load cell. The load cells have a capacity of 10 or 100 g with a resolution of ~ 0.01 g. Specimen load/stress and crosshead displacements are measured using a customized data acquisition program, while the specimen strain is calculated from SEM micrographs using an open source digital image correlation script developed by Eberl and coworkers for Matlab®. We use focused ion beam (FIB) machining to fabricate micro-compression and tension samples with minimum dimensions of 1-10 μm . Compression specimens typically have a uniform cross-section with a 2:1 aspect ratio while the tension samples are higher aspect ratio “dog-bone” specimens. In Fig. 5, we show the tensile response for a Pd-based metallic glass specimen loaded in tension. The inset SEM micrograph shows a typical tension specimen with a minimum gage width of ~ 2 μm and overall length of ~ 35 μm loaded in the grip. Tension and compression tests of AlON are pending; however, this metallic glass system has been used extensively in the development and validation of this custom in-situ SEM test stage. In future work, we will examine the strength and fracture behavior of single and bi-crystal specimens.

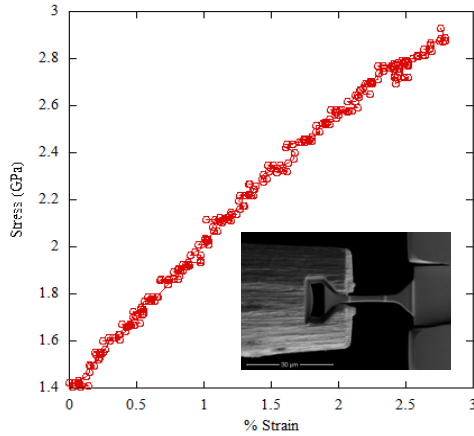


Fig. 5. Stress-strain response for a Pd-based metallic glass specimen loaded in tension. The inset shows an SEM micrograph of a FIB-machined dogbone specimen.

2.3 Coherent Gradient Sensing of Dynamic Fracture

Despite its long history, capturing relevant data and creating models for the dynamic failure of materials at the macro-scale is a non-trivial task. Material failure in the form of cracks or other localizations is a discrete event, reducing the effectiveness of many traditional material characterization testing techniques that rely on homogenization. Full-field data, particularly when over-driven cracks may bifurcate or a failure-mode transition might occur, is highly informative for observing phenomena as well as developing models for failure events.

The full-field method of coherent gradient sensing (CGS) (Tippur, 1991) was implemented at the Army Research Laboratory to study the dynamic fracture of transparent brittle materials. CGS is a full-field imaging technique that produces fringes based on the out-of-plane strain gradient, making it insensitive to noise and capable of discerning the tip of a crack when the crack-opening-displacement is small. Employing an 8-watt 532-nm wavelength laser coupled with a Cordin 222C-16 camera allows framing rates as high as 10-million frames per second (limited by laser power), which is critical in capturing cracks traveling several kilometers per second. Crack bifurcation in poly(methyl- methacrylate) (PMMA) at a nominal crack velocity of 745 m/s (Umberger, 2009) is shown in Fig. 6. CGS and the method of caustics have allowed observation of high-speed crack propagation in polymers, glasses, and ceramics, resulting in the computation of the dynamic fracture toughness as a function of crack speed for mixed-mode cracks common in ballistic penetration. Initial work with the transparent ceramic AION revealed decided thickness effects; ongoing work seeks to determine whether this effect is due to the material itself or the testing methodology.

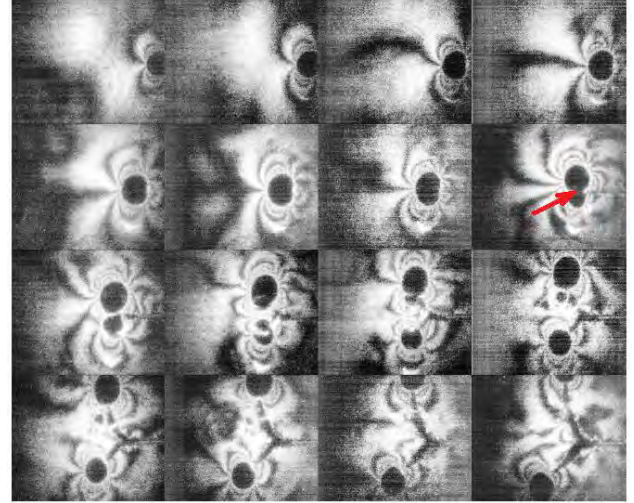


Fig. 6. CGS images of crack bifurcation (initiation indicated by red arrow) in PMMA.

Simulation of dynamic crack propagation at the macro-scale currently relies on the data obtained from the macro-scale laboratory tests discussed above along with the computational technique of the adaptive insertion of cohesive zones. The adaptive insertion of cohesive zones, pioneered by Ortiz and his co-workers (Camacho and Ortiz, 1996), allows the connectivity of the finite element mesh to be changed based on a specified failure criterion. Rate-dependent cohesive laws for the fracture of PMMA were developed and implemented into finite element codes featuring adaptive insertion based on the extensive experimentation documented in Umberger (2009). Current simulations can accurately predict crack propagation speeds and bifurcation; validation experiments to test the methodology with multiple mixed-mode cracks in a complex geometry have yielded positive, if mesh dependent, results. Ongoing experimental efforts with AION and the mesoscale work underway at ARL will hopefully provide a similar rate-dependent cohesive law and illuminate the crack propagation mechanisms (intra- versus inter-granular fracture, localized plasticity, et cetera) critical in predicting dynamic failure.

2.4 Shock Compression Experiments

Shock compression of AION has been reported by Cazamias et al. (2001) to 15 GPa, by Vaughan et al. (2001) to 21 GPa, by Sekine et al. (2003) from 61 to 180 GPa, and by Thornhill et al. (2006) from 5-89 GPa. These studies included the Hugoniot Elastic Limit (HEL), Hugoniot measurements to 180 GPa and phase transition, shear strength, and spall strength. The densities of AION used in the investigations of Cazamias et al. (2001) and Vaughan et al. (2001) varied between 3.51-3.59 Mg/m³.

The density of AlON used by Sekine et al. (2003) and by Thornhill et al. (2006) was 3.67 Mg/m^3 . Dandekar et al. (2007) analyzed the results of these shock compression investigations to determine the shear strength of AlON. The results of these studies may be summarized as follows: (i) The HEL of AlON varies between 10.5 and 12.1 GPa. (ii) The shear strength of AlON at the HEL range from 3.3 to 3.9 GPa. AlON continues to maintain shear strength between 4.4 and 6.0 GPa above the HEL even when the compression of AlON indicates a softening around 16.5 GPa. (iii) Sekine et al. (2003) observed a softening in compression around 50 GPa and postulated a phase transition for the reported shock compression of AlON around 130 GPa. (iv) Spall strength of low density AlON was reported to be 0.14 and 1.7 GPa for impact stress of 9.5 and 4.8 GPa (Cazamias et al., 2001). Thornhill et al. (2006) failed to detect any spall strength in AlON when shocked to 5.4, and 7.8 GPa, respectively. The compressive durations in two spall measurements each of Cazamias et al. (2001) and Thornhill et al. (2006) were 0.36 and 0.18 μs , and 0.35 and 1.16 μs , respectively.

The puzzling/inconclusive results of the previous spall experiments, lead us to postulate a hypothesis that the magnitude of spall strength of AlON is dependent on both shock induced compressive stress and its duration. A suite of experiments have been designed to test this hypothesis. The selected compression durations for these experiments are 0.18, 0.54, and 1. μs if needed. Spall behavior of AlON will be determined to 10 GPa with the two selected compression durations. Results of two spall experiments performed at 3.1 and 3.2 GPa are shown in Fig. 7. The compressive profiles show unexpected fluctuations. The reason for the observed fluctuations is not currently understood. Similar fluctuations were also present in previous studies (Thornhill et al., 2006).

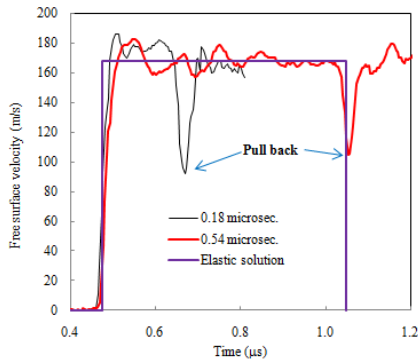


Fig. 7. Free surface velocity profiles in AlON.

The elastic solution provides the magnitude of fluctuations during the compression of AlON even though AlON remains globally elastic. The effect of duration of shock wave compression is clearly seen in these wave profiles. The magnitude of pull back velocity is larger for

the smaller duration of compression. The calculated values of spall strength of AlON when shocked to 3.1-3.2 GPa for the compression durations of 0.18 and 0.54 μs are 1.65 and 1.09 GPa, respectively i.e., a 33% decrease in the spall strength.

3. COMPUTATIONAL MODELING

3.1 Quantum Mechanics (QM)

The atomic structure and elastic properties of aluminum oxynitride spinel (AlON) at high pressure (up to 40 GPa) have been calculated from first principles. We have assumed an “ideal” stoichiometry of cubic AlON with 35.7 mole % AlN using the constant anion model (McCauley, 1978), and assuming an Al vacancy on the octahedral site. The elastic constants were calculated from independent strains that were applied to a unit cell, parameterizing the total energy as a function of the strain and from a stress-strain relationship. The methods gave quite close values of elastic constants, which indicate convergence of energy of cut-offs and total energy. The purpose of the calculations is to determine if the location and/or segregation of N atoms in the unit cell affects the elastic properties of AlON. The calculations have been carried out for two random (Fig. 8(a)) to clustered (Fig. 8(b)) arrangements of nitrogen atoms in the unit cell.

At ambient conditions a clustered distribution of N atoms has $\sim 1 \text{ eV}$ per 55 atoms higher total energy than for a random distribution and slightly, but systematically lower elastic constants. The pressure dependence of C_{11} , C_{12} and C_{44} for random and cluster distributions of N atoms was calculated in the range of 0-40 GPa by performing six finite distortions of the lattice and deriving the elastic constants from the strain-stress relationship. The calculated values of dC_{11}/dP are in the range of 4.0-6.2 and for $dC_{44}/dP \sim 0.8$ -1.5.

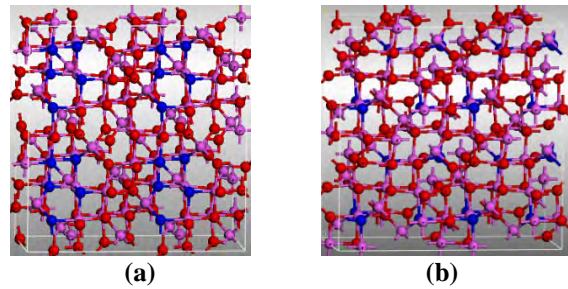


Fig. 8. Cluster (a) and random (b) distribution of nitrogen atoms over oxygen sites.

3.2 Molecular Dynamics (MD)

As MD simulations are to be used to explore failure mechanisms for AlON, it is crucial that the interaction

potential used in the MD simulations be assessed for suitability in describing this system. It is equally important that the simulation supercell adequately depicts the physical system. The interaction potential model we are using is based on the Buckingham potential

$$V(r_{ij}) = A_{ij} \exp\left(-\frac{r_{ij}}{\rho_{ij}}\right) - \frac{C_{ij}}{r_{ij}^6} + \frac{q_i q_j}{r_{ij}} \quad (1)$$

Polarization of the oxygen atoms is achieved via the shell model of Dick and Overhauser (1958).

3.2.1 Random Generation of Initial Configuration

In the constant anion model, about one-third of the aluminum atoms are located in tetrahedral coordination, the remaining aluminum atoms are found in octahedral sites, and one site remains vacant. First principles calculations (Fang et al., 2001) on an idealized unit cell (in which the vacancy and location of the N atoms are assumed) have demonstrated that the most stable structure of AION has the Al vacancy at the octahedral site, with six O nearest neighbors (VO_6). The positions of the five nitrogen atoms and the one vacancy in a 55-atom unit cell are not actually known nor are they unique. Anisotropic NPT simulations (in which angles between cell vectors were constrained to be orthogonal) of small supercells composed of repeating unit cells in which the locations of the vacancy and N atoms were the same produced crystals that were not cubic.

3.2.2 Size Effect of Cubicity

Ten systems of 1485 atoms were generated, as well as ten systems of 11880 atoms, in which the locations of the vacancies and N atoms are randomly selected. Each system was simulated in the N σ T ensemble, where both the simulation cell lengths (a , b and c) and the angles between cell vectors (α , β and γ) are unconstrained. If an individual system is cubic, such a simulation should result in the averaged simulation cell lengths being equal ($a = b = c$), and the angles orthogonal ($\alpha = \beta = \gamma = 90^\circ$). Fig. 9 shows the average cell dimensions ((a) and (b)) and cell angles ((c) and (d)) for the two system sizes. While no simulation cell ended up being purely cubic, increasing the system size clearly improves the cubicity of the system, as the data points get closer to the overall average values, with decreased error.

The cubic elastic constants, C_{11} , C_{12} and C_{44} , of AION have been predicted using QM and MD methods, and from these, Voigt averages (upper bounds) for Young's, E_v , shear, G_v , and bulk modulus, K_v , have been determined and compared with experimental values from polycrystals (Graham et al., 1988), (Table 1). The QM model contains either a random or cluster distribution of N atoms (Batyrev et al., 2009) resulting in the range of

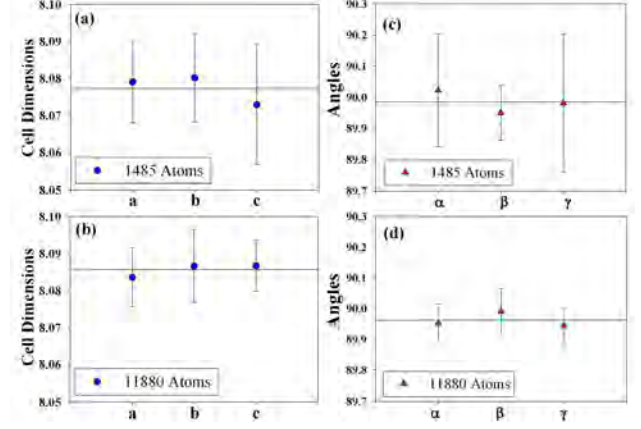


Fig. 9. Effect of system size on the cubicity of the simulation cell in which the locations of vacancies and N atoms are randomly selected within individual unit cells. Average cell dimensions are shown for the (a) small system and (b) large system, and the average cell angles of the (c) small system, and (d) large system, with standard error bars. The reference lines indicate the overall average values for that system size.

values shown in the Table 1. For MD systems consisting of 1485 atoms, both shell and no-shell configurations also predict a range in elastic constants. Voigt averages for the QM model more closely predict values obtained from polycrystals, and independent measurements of the elastic constants from single crystals of AION would aid in validating the QM and MD models presented here.

Table 1. AION elastic constants.

	QM	MD	Experiment
C_{11}	296-306	367-394	-
C_{12}	151-158	224-228	-
C_{44}	164-183	242-262	-
E_v	315-341	430-467	307-320
G_v	127-139	173-190	123-128
K_v	199-207	273-283	206-214

3.3 Single Crystal Dynamics

A continuum mechanics model for behavior of AION single crystals has been developed. Sections 3.3.1 and 3.3.2 summarize model features and results. A more complete description is forthcoming (Clayton, 2010).

3.3.1 Material Model

The structure of AION is presumed spinel, with cubic symmetry. Deformation gradient \mathbf{F} is

$$\mathbf{F} = \partial \mathbf{x} / \partial \mathbf{X} = \mathbf{F}^E \mathbf{F}^P, \quad (2)$$

where \mathbf{F}^E accounts for thermoelastic deformation and \mathbf{F}^P accounts for slip and twinning. Specifically,

$$\dot{\mathbf{F}}^P \mathbf{F}^{P-1} = \sum_i \dot{\gamma}^i \mathbf{s}^i \otimes \mathbf{m}^i + \sum_j \dot{\gamma}^j \gamma_T \mathbf{s}^j \otimes \mathbf{m}^j, \quad (3)$$

with $\dot{\gamma}^i$ the slip rate on system i , f^j the volume fraction of a material element that has undergone twinning on system j , s the slip or twinning direction, and m the unit normal to the plane of slip or twinning. For spinel, twinning shear $\gamma_T = 2^{-1/2}$. Slip and twin systems (Hornstra, 1960; Mitchell, 1999) are shown in Fig. 10.

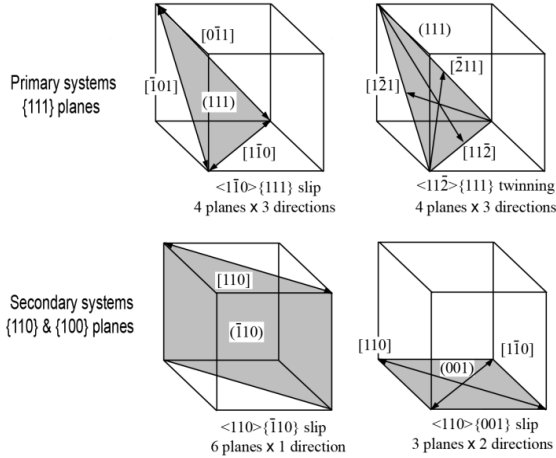


Fig. 10. Slip and twin systems in spinel ceramic crystals.

Nonlinear thermoelasticity of single crystals with defects is addressed. Helmholtz free energy density Ψ is

$$\Psi = \Psi(\mathbf{E}^E, \theta, \rho_\perp, \eta_T), \quad (4)$$

with $\mathbf{E}^E = (\mathbf{F}^{ET} \mathbf{F}^E - \mathbf{I})/2$ elastic strain, θ temperature, ρ_\perp dislocation density, and η_T twin boundary density. The explicit form of (4) includes anisotropic nonlinear thermoelasticity, dislocation line energy, and stacking fault/twin boundary energy (Clayton, 2009). Kinetic equations dictate slip rates and rates of twin volumes. Resistance to slip or twinning increases with shearing rate and dislocation density. Strength varies with temperature or pressure in proportion to the elastic shear modulus.

3.3.2 Model Calculations

Thermomechanical responses of AION single crystals and polycrystals subject to homogeneous field \mathbf{F} are studied. Loading pertinent to plate impact is considered: adiabatic uniaxial strain at a high rate ($10^5/\text{s}$). In Fig. 11, predicted axial stress σ (normalized by isentropic bulk modulus $K_0 = 216$ GPa) versus V/V_0 closely fits experimental data (Dandekar et al., 2007). Calculations for polycrystals reported in Fig. 11 require incorporation of nonlinear elasticity, self-consistent treatment of voids, and pore collapse with pressure. Void collapse results in the kink in the stress-volume curve for $0.96 > V/V_0 > 0.91$. The model overestimates axial stress in high pressure regime $V/V_0 < 0.88$, suggesting the pressure derivative of the bulk modulus under shock compression is lower than the value used in this model (Graham et al., 1988) and/or a need for elastic constants of even higher order.

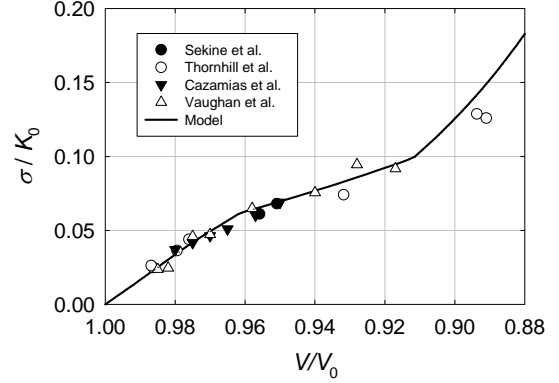


Fig. 11. Normalized axial stress in adiabatic uniaxial strain; data points for plate impact of AION polycrystals.

Because resistances to deformation mechanisms shown in Fig. 10 are not known a priori, several possibilities are explored: equal strengths of all systems, exclusive $\langle 110 \rangle \{111\}$ slip, preferred $\langle 110 \rangle \{110\}$ slip, and preferred $\langle 112 \rangle \{111\}$ twinning. Each is sufficient for matching experimental shear strength data (Dandekar et al., 2007). Representative slip and twin resistances τ_c are listed in Table 2, accounting for rate sensitivity at loading rate $\dot{\gamma}_0 = 10^5/\text{s}$ and normalized by tangent shear modulus μ , the latter ≈ 130 GPa at the HEL. Tabulated values are 1.4%-3.8% of the shear modulus, providing for post-HEL polycrystal shear strength ≈ 3 -4 GPa. When extrapolated to the quasi-static limit, shear resistances are comparable to values for other spinel (Mitchell, 1999) and to Peierls stresses for full dislocations on $\{111\}$ planes. Such extrapolation may underestimate strength in the static limit because rate sensitivity tends to decrease with decreasing rate as drag mechanisms decline.

Table 2. Dynamic strengths of slip and twin systems.

Model System	Normalized shear strength τ_c / μ			
	All Equal	Exclusive {111} slip	Preferred {110} slip	Preferred twinning
{111} slip	0.026	0.019	0.029	0.038
{110} slip	0.026	∞	0.014	0.038
{100} slip	0.026	∞	0.029	0.038
{111} twin	0.026	∞	0.029	0.019

Calculations for single crystals compressed along $[100]$ and $[110]$ demonstrate that maximum shear stresses can vary by over a factor of two at compression corresponding to the polycrystal HEL ($V/V_0 \approx 0.97$) depending on lattice orientation and choice of model from Table 2.

3.4 Mesoscale Model

The mesoscopic length scale is treated using parallel, three-dimensional finite elements with microcracks explicitly represented on the grain boundaries using

cohesive interface laws allowing investigation of crack nucleation, growth, and coalescence. The basis of our model is the Lagrangian approach and finite element meshes representing computational microstructures are constructed using Voronoi tessellation and a Monte Carlo-based grain growth approach (Rollett and Manohar, 2004; Wu and Sullivan, 2003; Kuprat (2000).

The volume-meshed microstructures consist of grains, which are treated as separate bodies in a multi-body contact/interface algorithm. Currently, only isotropic linear elasticity is being used for the bulk grain material. In the future, anisotropic linear elasticity and crystal plasticity, discussed in Section 3.3 will be used based on results of density functional theory calculations of AION for elastic constants discussed in Sections 3.1 and 3.2. Microcracks are modeled using cohesive interface laws, where a relationship exists between traction and separation of two surfaces at an interface. Numerically, the imposed stress distribution eliminates the stress singularity at the “real” crack tip by imposing tractions across a “virtual” crack tip, acting to close the crack. The imposed distribution relates the crack opening displacement and tractions and is referred to as a cohesive law. In this work a linear-decreasing cohesive law is used.

For the 50-grain simulations, specimens were loaded with a range of constant strain rates. During the initial stages of building the three-dimensional computational framework, the microstructures were loaded so that the top boundary of the mesh was moved at a constant velocity of 0.2 m/s, or $\dot{\epsilon}_{nom} = 0.20 \text{ m/s} / 0.002 \text{ m} = 100 \text{ s}^{-1}$. Since a sudden velocity impulse is imposed on the microstructure, this corresponds to a shock loading. Other boundary conditions could be applied as needed, such as confinement loading. Fig. 12 shows the engineering stress-strain response for 50 grain loading in tension and compression. As expected, when loaded in tension the failure strength is approximately 307 MPa (a model input). In contrast, the peak compressive strength is 871 MPa at $\dot{\epsilon}_{nom} = 100 \text{ s}^{-1}$. This is an interesting result because Paliwal et al. (2006) measured 720 MPa at quasi-static loading rates ($\dot{\epsilon}_{nom} = 10^3 \text{ s}^{-1}$).

Contour plots of stress in the Y-direction (loading axis) of the compression simulation at various times are shown in Fig. 13. At 27.66 μs , stress concentrations at grain boundaries and triple junctions are pronounced until 32.45 μs when a multiple cracks are activated and begin to open. Once cracks are activated and begin to propagate, it is not until 35 μs , or 2.55 μs later that the compressive peak strength is reached. It is interesting to note that at peak stress (which would occur somewhere between 34.58 and 35.64 μs in the shown contour plots) the maximum crack density (all grain boundaries fractured) is

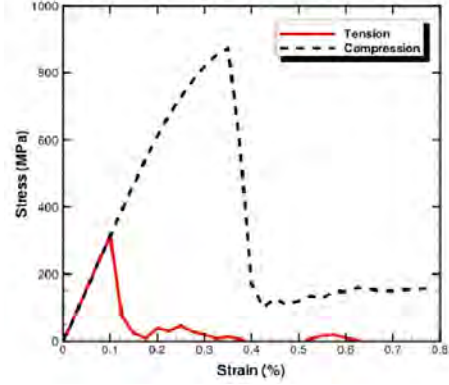


Fig. 12. 50-grain simulation in tension and compression.

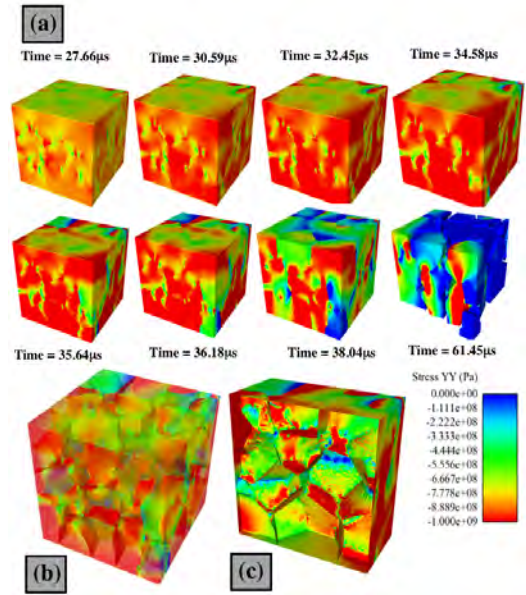


Fig. 13. Stress contour results in a 50-grain simulation.

not reached. Fig. 13(b) shows an image of the microstructure at 35.64 μs rendered transparent to show how most of the grain boundaries are still carrying load (have high stress, colored red). This is also evident in Fig. 13(c), which shows a cross section of the microstructure also at 35.64 μs .

CONCLUSIONS

Multiscale modeling of ceramics can provide valuable tools to understand the mechanics and physics of the brittle material inelastic response. Experimental observations at each of the spatiotemporal scales shown in Fig. 1 can be used for validation of the computational models developed at that scale. More specifically, interfacial grain boundary properties and estimated quasi-static strengths of slip and twin systems (Table 2), can be quantitatively determined using FIB/SEM tests on AION

single and bi-crystals. QM and MD models were used to predict the cubic elastic constants of AlON, yet validation of these models awaits experiments on large single crystals of AlON. This work demonstrated 3-D mesoscale simulations with fracture explicitly represented using cohesive zone models; such models can be validated using CGS methods for measuring dynamic crack propagation rates and bifurcation phenomena. Although the individual models for the hierarchical multiscale model for AlON are still being combined into a coherent framework, this work established the feasibility of the approach and the process for development of a virtual failure model for brittle materials (Fig. 12). Future work is aimed at development of a fully-concurrent multiscale model for brittle materials for “top-down” computational design of armor ceramics.

REFERENCES

- Batyrev, I. G., Rice, B. M., McCauley, J. W., 2009: First Principles Calculations of Nitrogen Atomic Position Effects on Elastic Properties of aluminum Oxynitride (AlON) Spinel, MRS Fall Meeting, Boston, MA.
- Camacho, G. T., Ortiz, M., 1996: Computational Modeling of Impact Damage in Brittle Materials, *Int. J. Solids Structures*, **33**, 2899-2938.
- Cazamias, J. U., Fiske, P. S., Bless, S. J., 2001: Shock Properties of AlON, in: Fundamental Issues and Applications of Shock-Wave and High-Strain-Rate Phenomena, Eds. K.P. Staudhammer, L.E. Murr, and M.A. Meyers, Elsevier, New York, 181-188.
- Clayton, J. D., 2009: A Continuum Description of Nonlinear Elasticity, Slip and Twinning, with Application to Sapphire, *Proc. R. Soc. Lond. A*, **465**, 307-334.
- Clayton, J. D., 2010: A Nonlinear Thermomechanical Model of Spinel Ceramics Applied to Aluminum Oxynitride, *ASME J. Appl. Mech.*, to appear.
- Dandekar, D. P., Vaughan, B. A. M., Proud, W. G., 2007: Shear Strength of Aluminum Oxynitride, In: *Shock Compression of Condensed Matter*, AIP Press, Melville, N. Y., 505-508.
- Dick, B. G., Overhauser, A. W., 1958: Theory of the Dielectric Constants of Alkali Halide Crystals, *Phys. Rev.*, **112**, 90-103.
- Fang, C. M., Metselaar, R., Hintzen, H. T., de With, G., 2001: Structure Models for γ -aluminum Oxynitride from *Ab Initio* Calculations, *J. Am. Ceram. Soc.*, **84**, 2633-37.
- Graham, E. K., Munly, W. C., McCauley, J. W., Corbin, N. D., 1988: Elastic Properties of Polycrystalline Aluminum Oxynitride Spinel and Their Dependence on Pressure, Temperature, and Composition, *J. Amer. Ceram. Soc.*, **71**, 807-812.
- Hornstra, J., 1960: Dislocations, Stacking Faults, and Twins in the Spinel Structure, *J. Phys. Chem. Solids*, **15**, 311-323.
- Kuprat, A., 2000: Modeling Microstructure Evolution Using Gradient-weighted Moving Finite Elements. *SIAM Journal of Scientific Computing*, **22**(2):535-560.
- Lundberg, P., Andersson, O., 2010: Experimental Study of the Dwell-Penetration Transition in SiC-X1 and AlON, Final report, FOI-2009-1179, FOI, Swedish Defence Research Agency.
- McCauley, J. W., 1978: A Simple Model for Aluminum Oxynitride Spinel, *J. Am. Ceram. Soc.*, **61**, 372-3.
- Mitchell, T. E., 1999: Dislocations and Mechanical Properties of MgO-Al₂O₃ Spinel Single Crystals, *J. Amer. Ceram. Soc.*, **82**, 3305-3316.
- Paliwal, B., Ramesh, K. T., McCauley, J. W., 2006: Direct Observation of the Dynamic Compressive Failure of a Transparent Polycrystalline Ceramic (AlON). *J. Amer. Ceram. Soc.*, **7**, 2128-2133.
- Rollett, A. D., Manohar, P., 2004: Monte Carlo Modeling of Grain Growth and Recrystallization, In: *Continuum Scale Simulation of Engineering Materials*, Eds. D. Raabe and F. Roters, Wiley-VCH, Ch. 4, page 855.
- Sekine, T., Li, X., Kobayashi, T., Yamashita, Y., Patel, P., McCauley, J. W., 2003: Aluminum Oxynitride at Pressures up to 180 GPa, *J. Appl. Phys.*, **94**, 4803-4806.
- Strassburger, E., Patel, P., McCauley, J. W., Kovalchick, C., Ramesh, K. T., Templeton, D. W., 2006: High-speed Transmission Shadowgraphic and Dynamic Photoelasticity Study of Stress Wave and Impact Damage Propagation in Transparent Materials and Laminates Using the Edge-on Impact (EOI) Method, Proceedings of the 25th Army Science Conference, Orlando, FL, Eds. J.A. Parmentola and A.M. Rajendran, Tech Science Press, 227 – 233.
- Thornhill, T. F., Vogler, T. J., Reinhart, W. D., Chhabildas, L.C., 2006: Polycrystalline Aluminum Oxynitride Hugoniot and Optical Properties, In: *Shock Compression of Condensed Matter*, AIP Press, Melville, N.Y., 143-146.
- Tippur, H. V., Krishnaswamy, S., Rosakis, A. J. 1991: A Coherent Gradient Sensor for Crack Tip Deformation Measurements – Analysis and Experimental Results, *Int. J. Fracture*, **48**, 193-204.
- Umberger, P., 2009: Experimental Evaluation of Dynamic Crack Branching in Poly(methyl methacrylate) Using the Method of Coherent Gradient Sensing. *US Army Research Laboratory Contractor Report ARL-CR-637*, Aberdeen Proving Ground, MD.
- Vaughan, B. A. M., Proud, W. G., Field, J. E., 2001: Shock Properties of Aluminum Oxynitride, Shock Physics, Cavendish Laboratory Report SP/1092.
- Wu, Z., Sullivan, J. M., 2003: Multiple Material Marching Cubes Algorithm. *Int. J. Numer. Meth. Eng.*, **58**(2), 189-207.

NO. OF
COPIES ORGANIZATION

1 (PDF only)	DEFENSE TECHNICAL INFORMATION CTR DTIC OCA 8725 JOHN J KINGMAN RD STE 0944 FORT BELVOIR VA 22060-6218
1	DIRECTOR US ARMY RESEARCH LAB IMNE ALC HRR 2800 POWDER MILL RD ADELPHI MD 20783-1197
1	DIRECTOR US ARMY RESEARCH LAB RDRL CIO LL 2800 POWDER MILL RD ADELPHI MD 20783-1197
1	DIRECTOR US ARMY RESEARCH LAB RDRL CIO MT 2800 POWDER MILL RD ADELPHI MD 20783-1197
1	DIRECTOR US ARMY RESEARCH LAB RDRL D 2800 POWDER MILL RD ADELPHI MD 20783-1197

<u>NO. OF COPIES</u>	<u>ORGANIZATION</u>
2	NSF S MCKNIGHT G PAULINO 4201 WILSON BLVD STE 545 ARLINGTON VA 22230-0002
2	DARPA W COBLENZ J GOLDWASSER 3701 N FAIRFAX DR ARLINGTON VA 22203-1714
2	US ARMY TARDEC AMSTRA TR R MS 263 K BISHNOI D TEMPLETON MS 263 WARREN MI 48397-5000
1	COMMANDER US ARMY RSRCH OFC RDRL ROE M D STEPP PO BOX 12211 RESEARCH TRIANGLE PARK NC 27709-2211
5	SOUTHWEST RSRCH INST C ANDERSON K DANNEMANN T HOLMQUIST G JOHNSON J WALKER PO DRAWER 28510 SAN ANTONIO TX 78284
1	UNIVERSITY OF MISSISSIPPI DEPT OF MECH ENGRG A M RAJENDRAN 201-B CARRIER HALL UNIVERSITY MS 38677
2	SRI INTERNATIONAL D CURRAN D SHOCKEY 333 RAVENSWOOD AVE MENLO PARK CA 94025

<u>NO. OF COPIES</u>	<u>ORGANIZATION</u>
1	VIRGINIA POLYTECHNIC INST COLLEGE OF ENGRG R BATRA BLACKSBURG VA 24061-0219
1	JOHNS HOPKINS UNIV DEPT OF MECH ENGRG K T RAMESH LATROBE 122 BALTIMORE MD 21218
1	INST OF ADVANCED TECH UNIV OF TX AUSTIN S BLESS 3925 W BRAKER LN STE 400 AUSTIN TX 78759-5316
1	APPLIED RSCH ASSOCIATES D E GRADY 4300 SAN MATEO BLVD NE STE A220 ALBUQUERQUE NM 87110
1	INTERNATIONAL RSRCH ASSOC INC D L ORPHAL 4450 BLACK AVE PLEASANTON CA 94566
2	WASHINGTON ST UNIV INST OF SHOCK PHYSICS Y M GUPTA J ASAY PULLMAN WA 99164-2814
1	UNIV OF DAYTON RSRCH INST N S BRAR 300 COLLEGE PARK MS SPC 1911 DAYTON OH 45469
1	MIT DEPT ARNTCS ASTRNTCS R RADOVITZKY 77 MASSACHUSETTS AVE CAMBRIDGE MA 02139

NO. OF
COPIES ORGANIZATION

75 ABERDEEN PROVING GROUND
DIR USARL
RDRL WM
B FORCH
S KARNA
J MCCAULEY
P PLOSTINS
M ZOLTOSKI
RDRL WML
J NEWILL
RDRL WML B
I BATYREV
B RICE
N WEINGARTEN
RDRL WML D
P CONROY
M NUSCA
RDRL WML F
D LYONS
RDRL WML G
M BERMAN
W DRYSDALE
RDRL WML H
D SCHEFFLER
S SCHRAML
B SCHUSTER
RDRL WMM
J BEATTY
R DOWDING
RDRL WMM A
J SANDS
J TZENG
E WETZEL
RDRL WMM B
T BOGETTI
B CHEESEMAN
C FOUNTZOULAS
G GAZONAS
D HOPKINS
R KARKKAINEN
P MOY
B POWERS
C RANDOW
T SANO
M VANLANDINGHAM
R WILDMAN
C F YEN
RDRL WMM D
E CHIN
K CHO
R HOWELL
RDRL WMM E
J ADAMS

NO. OF
COPIES ORGANIZATION

M COLE
T JESSEN
J LASALVIA
P PATEL
J SINGH
RDRL WMM F
L KECSKES
H MAUPIN
RDRL WMM G
J ANDZELM
A RAWLETT
RDRL WMP
P BAKER
S SCHOENFELD
RDRL WMP B
R BECKER
S BILYK
D CASEM
J CLAYTON
D DANDEKAR
M GREENFIELD
C HOPPEL
R KRAFT
B LEAVY
M RAFTENBERG
S SATAPATHY
M SCHEIDLER
T WEERASOORIYA
RDRL WMP C
T BJERKE
S SEGLETES
RDRL WMP D
R DONEY
D KLEPONIS
H MEYER
J RUNYEON
B SCOTT
RDRL WMP E
M BURKINS
B LOVE
RDRL WMP F
A FRYDMAN
N GNIAZDOWSKI
R GUPTA

INTENTIONALLY LEFT BLANK.